Vulnerability of masonry structures to settlement loading: a numerical DEM investigation

N. Savalle[1,2] , **Paulo B. Lourenço**[2], **P. Breul**[1]

[1] Université Clermont Auvergne, Clermont Auvergne INP, CNRS, Institut Pascal, F-63000 Clermont–Ferrand, France

[2] University of Minho, ISISE, Department of Civil Engineering, Guimarães, Portugal

Corresponding author: N. Savalle (e-mail: nathanael.savalle@uca.fr)

ABSTRACT Masonry is one of the oldest building materials. In addition, it is widespread and highly represented all over the world. Masonry structures can be subjected to various loading, including earthquakes, floods, winds, or soil settlements. On the other hand, climate change leads to dryer summers and wetter winters which, consequently, leads to more pronounced soil differential settlements. Today, the response of masonry buildings to soil settlements is still not completely understood and predictable, which threaten these constructions that hold both an economical (operational) and cultural value. In particular, the overall stiffness of masonry structures when subjected to settlements requires further investigations. The present work aims at calibrating a numerical discrete element model on existing settlement experiments. It discusses the pros, the cons, and the methodology to follow for a discrete element modelling of such systems.

Keywords masonry, settlements, dry-joint, stiffness, discrete element modelling

I. INTRODUCTION

Thousands of years ago, the humankind started to settle down and the first cities, which were very modest at that time, began to be constructed. As shown in archaeological sites, masonry was the first building material used to erect houses, burial, temples and community places, etc (Mithen 2011, Ramírez et al. 2015, Ard et al. 2015, Cousseau 2016). Today, masonry buildings still represent a significant part of the building stock (Jaiswal & Wald 2008). As a matter of fact, many emblematic cultural sites are shaped by masonry structures, such as religious monuments (churches, mosque), European city centres, vestiges from past civilisations (e.g. the city of Machu Picchu, the Great Wall of China, the pyramids of Egypt, among others), and rural areas litterally shaped by masonry (e.g. the Douro's Valley in Portugal, the Lavaux Terraces in Switzerland or the Baljenac Island in Croatia). To summarise, they compose the heritage of past and current civilisations and constitute a high cultural value, materialised by the UNESCO inscription of several masonry monuments and sites as well as some European historic city centres. This cultural value also leads to economical assets through tourism, as Europe still represents the world's number one tourist destination with 40% of arrivals in the world that accounts for 10% of the European GDP (European Comission 2010). In addition, these masonry buildings are often still in use and thus hold an economical (operational) value by essence.

Masonry buildings can suffer from extreme events such as earthquakes (Vlachakis et al. 2020, Stepinac et al. 2021) and floods (Xiao et al. 2021), yet structural damage can also occur more progressively because of soil settlement that can produce differential settlements on the foundation or the abutments (Alessandri et al. 2015, Hemeda 2021, Funari et al. 2021). In particular, their vulnerability to soil settlement is high as masonry is a very brittle material, which leads to visible cracks in walls, arches and vaults. Often, the interventions are based on a continuous monitoring and engineering judgement (Masciotta et al. 2017, Ceravolo et al. 2017). But in practice, the level of safety of cracked masonry structures is often hard to estimate. For this reason, the research community is devoted to the understanding of the underlying phenomena behind settlement loading and the development of numerical models dedicated to such structural issues. In fact, in-field studies succeed to calibrate the elastic properties of the system to reproduce the current state of the examined masonry structures (Alessandri et al. 2015, Funari et al. 2021), without, however, the certainty of being able to predict the evolution with a more, or alternatively, less, pronounced soil settlement. For this reason, the research community needs a combination of in-field studies and experimental tests that provide more complete data sets, for validation purposes.

From a general point of view, the response of masonry structures to settlement loading must include the soil-structure interactions as the behaviour of the two sub-systems is highly correlated (Deck & Singh 2012, D'Altri et al. 2019). However, in practice, given the high complexity of such tests (Ritter et al. 2018, Laefer et al. 2011, Dalgic et al. 2021), experimental studies tend to simplify the soil response using predefined foundation settlements and instead focus on the masonry response (Giardina et al. 2012, Portioli & Cascini 2016, Bui et al. 2017, Portioli & Cascini 2017, Giardina et al. 2020, Gagliardo et al. 2021, Savalle et al. 2023). Such experimental data then serves as a validation framework for numerical tools (Giardina et al. 2013, Portioli & Cascini 2016, Bui et al. 2017, Giardina et al. 2020, Chen et al. 2021, Gagliardo et al. 2021). The comparisons can either concern only the crack patterns (between the experiments and the numerical models) (Bui et al. 2017, Chen et al. 2021). Alternatively, when the vertical load-displacement curves are also compared between experiments and numerical models, the agreement is often not ideal (Portioli & Cascini 2017, Giardina et al. 2020, Gagliardo et al. 2021), unveiling research needs to understand the driving parameters of the response of masonry structures to settlement.

The present article aims to understand the effect of structural parameters (in particular the joint stiffness) on the response of masonry structures to settlement. In particular, it builds on existing experiments on several masonry walls that provide the vertical load-displacement curves (Savalle et al. 2023). Importantly, it uses dry-joint masonry structures as heritage masonry structures are commonly modelled as dry jointed since, at the time of the construction, mortar was either lacking or very weak and disappeared through age and weathering (Portioli & Cascini 2017, Colombo et al. 2022). In addition, masonry being very brittle, for weak mortars, cracks rapidly develop in the joints (Milani et al. 2013) leading to a dry-joint behaviour in the large displacements regime. Since dry-joint masonry is considered, the present work employs the discrete element method as it is commonly used in such cases (Bui et al. 2017, Chen et al. 2021, Colombo et al. 2022, Savalle et al. 2022). The first part briefly presents the experiments that serve as a validation framework (Savalle et al. 2023). Then, the numerical strategy is detailed, with the emphasis on the driving parameters with some parametric analysis. After, the numerical results are compared with the experimental ones and finally some conclusions are drawn.

II. Description of the experimental campaign

This section briefly introduces an existing experimental campaign on masonry shear walls (Savalle et al. 2023) that will be used later on for comparison purposes with numerical results. The campaign consist of a masonry wall composed of eight courses of masonry units, arranged in a running bond pattern with eight full units composing the even courses (Figure 1). The first course is completely fixed in all directions while the rest of the units are free to move. The units are made of calcium silicate material and have a unit weight

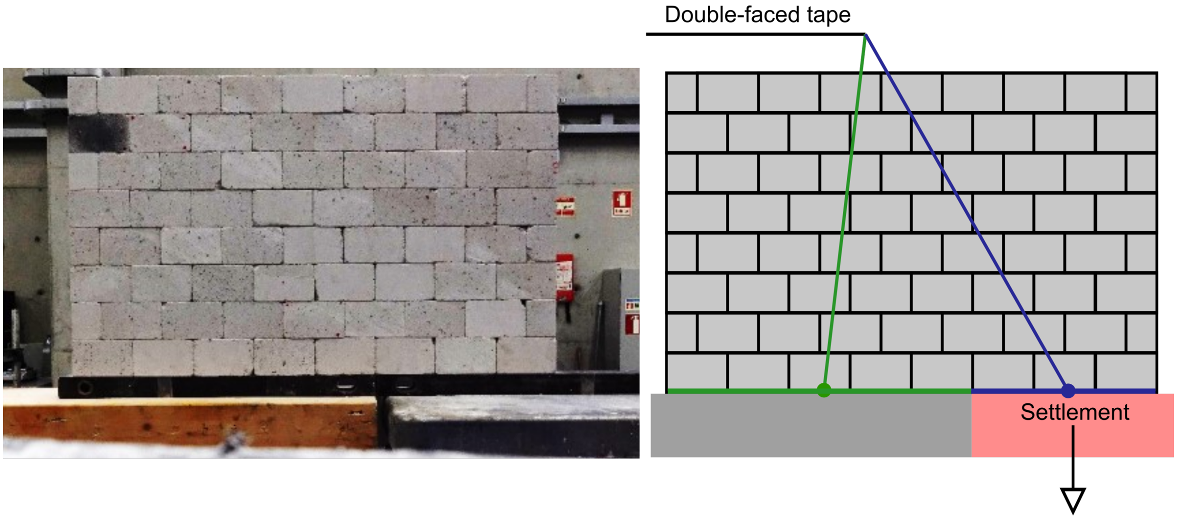

FIGURE 1. Settlement experiments (Savalle et al. 2023): the shear wall is visible on the left while the principle of the settlement experiment is explained on the right.

of $18.4\mathrm{kN}\cdot\mathrm{m}^{-3}$, a Young's modulus of $E = 7.0\mathrm{GPa}$ and a compressive strength of $36.5\mathrm{MPa}$ (Colombo et al. 2022). They are $70.3\mathrm{mm}$ high, $114.9\mathrm{mm}$ long and $57.3\mathrm{mm}$ thick which also corresponds to the thickness of the shear walls (third dimension non visible in Figure 1), leading to a wall height of $562\mathrm{mm}$ and wall length of $574\mathrm{mm}$. Finally, the interface properties (friction angle φ, interface normal k_n and tangential k_s stiffness) and have been characterised in Colombo et al. (2022). The friction angle has been evaluated to $33.4°$, while the normal and tangential stiffness of a dry-joint between two blocks have been found equal to $k_n = 1.14\mathrm{GPa}\cdot\mathrm{m}^{-1}$ and $k_s = 0.33\mathrm{GPa}\cdot\mathrm{m}^{-1}$. A detailed discussion about these parameters is presented in Section 4.1.

As shown in Figure 1, one part of the wall is resting on a fixed platform (grey area), while the other one is subjected to a vertical, here predefined, settlement (light red area). The proportion of the wall subjected to settlement was varied along the experimental campaign, with four configurations in total corresponding to one fourth, three eighth (the case in Figure 1), a half and five eighth of the wall. The vertically predefined settlement was slow as to leave the wall always in a quasi-static regime, while both the vertical load and vertical displacement were measured. Finally, each configuration was tested three times (five times for the case shown in Figure 1) for repeatability purposes. The aim of the next sections is to define a numerical methodology able to replicate the experimental outcomes.

III. Numerical methodology

The present section details a 3D Discrete Element Model (DEM) of the experiments presented in Savalle et al. (2023). Though the mechanisms displayed by the experiments are mainly 2D, a 3D model is preferred here in order to also allow the out-of-plane rotations of the blocks that actually occurred for some blocks in the upper part of the walls. As stated in the introduction, dry-joint systems are often modelled through discrete element approaches (Bui et al. 2017, Chen et al. 2021, Colombo et al. 2022). Indeed, their response is mainly driven by the large displacements occurring between units at the interfaces (Alexandris et al. 2004), while the units can reasonably be assumed rigid. In the present case of the experiments above, it is easy to compare the stiffness of both the units and the dry-joints. For the dry-joint, it gives $k_n = 1.14\mathrm{GPa} \cdot \mathrm{m}^{-1}$, while for the unit, it becomes $E/L = 60.9\mathrm{GPa} \cdot \mathrm{m}^{-1}$, with L being the longest dimension of the units. From this comparison, it is clear that the deformability of the units is far negligible and thus justifies the rigidity assumption.

A. Generalities of Discrete Element Methods (DEM)

Since the first developments of a numerical procedure to study assemblies of rigid blocks proposed by Cundall (1971), different formulations, with different names, have been introduced through years (among others, the distinct element approach, the discontinuous deformation analysis, the rigid block analysis) (Lemos 2007). While most of them currently allow the study of deformable bodies, one of their common aspects is that they are able to study the mechanics of rigid bodies assemblies, which corresponds to the framework of the focused experiments. Another common characteristic of the Discrete Element Methods (DEM) is that they also allow full separation between bodies, associated with dedicated contact formulations, thus allowing large displacements to occur. In turn, this requires the usage of an explicit algorithm with an appropriate time-step to solve the equations of motion (Lemos 2007). However, today, one can note that the differences between finite element and discrete element software are becoming tinier, with for instance the ability to use an explicit or implicit solver in Abaqus (2014) or to use deformable blocks and/or small strains in 3DEC (Itasca 2019). In the present work, the numerical strategy is developed using the 3DEC environment commercialised by Itasca company (Itasca 2019).

B. Explicit algorithm to solve the equations of motion

This subsection describes the explicit algorithm followed by 3DEC to solve the equations of motion in case of rigid bodies. For deformable bodies, intermediary steps to compute stresses and strains are added to the information provided below (Itasca 2019). Since the model is developed in 3D, each unit of the masonry shear wall is represented by a rigid body with six degrees of freedom (three translations and three rotations) expressed at its centre of mass and is subjected to two types of forces. First, the body forces (e.g. gravity) are applied at the centre of mass of the unit. Then, the contact forces are transmitted by neighboured units through interfaces represented by zero-thickness springs (either linear or non-linear depending on the constitutive law of the interface). Therefore, since the bodies are rigid, those interfaces concentrate all the deformability of the model. In 3DEC, contact interfaces are automatically created once two bodies are in contact (i.e., determined to be close enough by an internal routine). Block faces are then triangulated to create contact points (also called subcontacts). By default, contact points are generated at each vertex of the block faces, however, the user can use a more refined triangulation to create more contact points (see Section 4.2). It is important to notice that contact forces are only transmitted through these contacting points, in a (more or less refined) discrete manner. Each contact point (subcontact) is then associated to an area computed as one-third of the areas of the triangles containing this point. To summarise, each unit i, of mass m_i and moments of inertia I_i is subjected to n_i forces (body and contact forces) F_i^j that produces n_i moments M_i^j. The explicit algorithm requires a time-stepping approach: at a given step, all forces and their moments are known and the acceleration a_i and angular acceleration $\ddot{\theta}_i$ of each unit i are computed thanks to the simplified equations of motion, in particular removing the non-linear terms $(I_i^3 - I_i^2)\dot{\theta}_i^2\dot{\theta}_i^3$ as the velocities

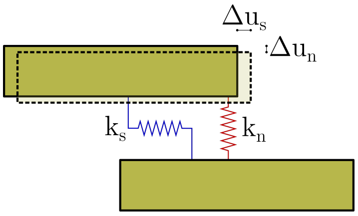

FIGURE 2. Idealised schematic view of the contact between two units in 3DEC. The two springs k_n and k_s produce forces under incremental displacements Δu_n and Δu_s.

$\dot{\theta}_i^2$ and $\dot{\theta}_i^3$ are always small.

$$\begin{aligned} m_i a_i &= \sum_j^{n_i} F_i^j \\ I_i \ddot{\theta}_i &= \sum_j^{n_i} M_i^j \end{aligned} \tag{1}$$

In order to describe the three rotations and displacements of each unit (degree of freedom), one can note that I_i is a 3D diagonal matrix (expressed in the principal base of block i) and a_i, F_i^j, $\ddot{\theta}_i$, M_i^j, and $I_i\ddot{\theta}_i$ are 3D vectors.

Once the accelerations are known at a step t, the velocities v_i and positions u_i are integrated through a central difference algorithm to describe the system at a step $t + \Delta t$, Δt being the numerical time-step (small enough to ensure numerical stability) of the simulation. The latter is automatically calculated by the program and is taken as a proportion (0.8 by default) of the critical time-step. The critical time-step is computed as twice the square root of the ratio between the smallest nodal mass (equivalent to the smallest mass of one rigid block) and the maximum contact stiffness in the system (expressed in $\mathrm{N} \cdot \mathrm{m}^{-1}$). Mass-scaling can artificially increase the mass of small rigid blocks in order to decrease the critical time-step. However, in the present simulations, the smallest blocks (the half-blocks at the two end of the odd courses) are not small enough to induce any significant modification on the numerical time-step. The equation below describes the computation of the position of the centre of mass of each unit only for brevity, though an identical procedure is used to integrate the angular accelerations to solve the orientation of each unit.

$$\begin{aligned} v_i\left(t + \frac{\Delta t}{2}\right) &= v_i\left(t - \frac{\Delta t}{2}\right) + a_i\left(t\right) \cdot \Delta t \\ u_i\left(t + \Delta t\right) &= u_i\left(t\right) + v_i\left(t + \frac{\Delta t}{2}\right) \cdot \Delta t \end{aligned} \tag{2}$$

The new positions (and orientations) of each unit provokes incremental relative displacements at the contact interfaces between units, which, in turn, modifies the contact forces transmitted through these contacts. If Δu_n and Δu_s denote the normal and tangential relative displacement increments at a given contact point, the increments of normal ΔF_n and tangential ΔF_s contact forces are computed through the following formula (Figure 2).

$$\begin{aligned} \Delta F_n &= k_n \cdot A_c \cdot \Delta u_n \\ \Delta F_s &= k_s \cdot A_c \cdot \Delta u_s \end{aligned} \tag{3}$$

In the equation above, k_n, k_s and A_c denote the normal and tangential stiffness and the area of contact of the considered contact point, respectively. As the number of contact points (and therefore the associ-

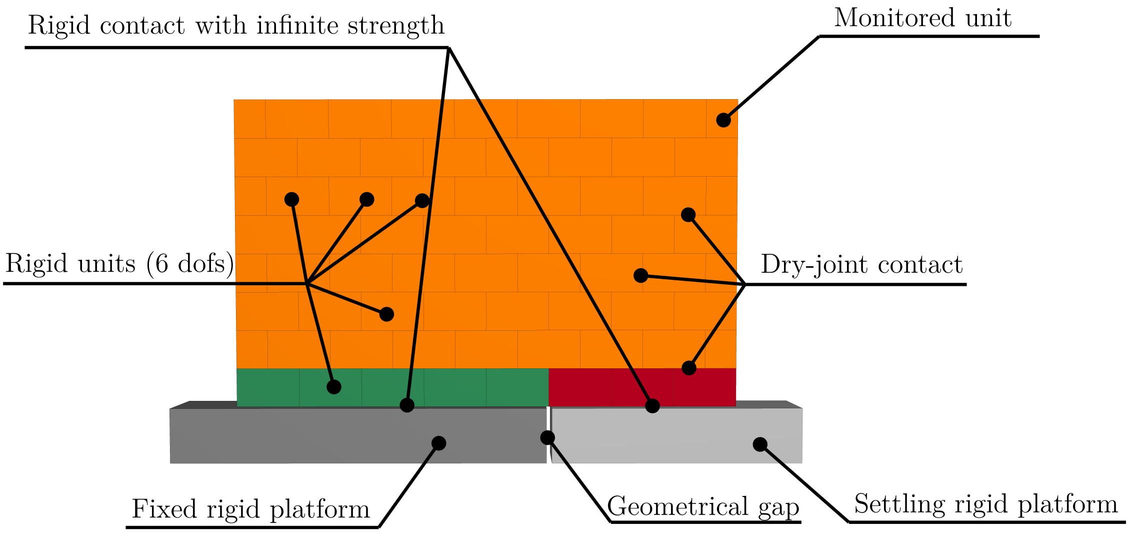

FIGURE 3. Numerical model with detailed boundary conditions and contacts between rigid bodies, in the case of three units on the settling platform.

ated contact areas A_c) depends on the triangulation of the surface, one needs to optimise it. A too high number of contact points will increase the numerical cost of each time-step, while a too low number will jeopardise the accuracy of the computation. In practice, enough contact points (usually around 5) ensure an accurate transmission of forces between units (Lemos 2019, Savalle et al. 2022) and herein, the number of contact points will be defined later on for the special case of these simulations (Section 4.2). For elastic contacts (infinite strength), the incremental contact forces are simply integrated through the equation $F_{n,s}(t+\Delta t) = F_{n,s}(t) + \Delta F_{n,s}$. However, in the current context of dry-joint masonry walls, sliding failure can occur between units. Therefore, the contact forces are ruled by the Mohr-Coulomb constitutive law which limits the tangential forces. Assuming φ and C the friction angle and the cohesion (here null as the contact is dry) of the contact, respectively, it becomes:

$$\begin{aligned} F_n(t+\Delta t) &= F_n(t) + \Delta F_n \\ F_s(t+\Delta t) &= min\left[F_s(t) + \Delta F_s, F_{s,max}\right] \\ F_{s,max} &= CA_c + F_n \cdot \tan(\varphi) \end{aligned} \tag{4}$$

Note that in both cases (elastic or Mohr-Coulomb contact), tension failure, i.e. detachment when F_n goes to 0, is possible. Finally, for quasi-static simulation which is the case here, the computations is sped up thanks to an artificial numerical damping (Bui et al. 2017, Itasca 2019, Savalle et al. 2020, 2022, Colombo et al. 2022). In fact, at each time-step, an additional damping force is used to reduce the unbalanced forces, in a similar manner to dynamic relaxation in order to find the equilibrium faster. As recommended by the authors above, a value of 0.8 is chosen herein for the mechanical damping.

C. Boundary conditions

Figure 3 displays an example of the numerical geometrical model employed in this work. All masonry units in the shear wall (orange units) are free to move as it was the case in the experiments. It is recalled

TABLE 1. Increments of vertical displacement between two consecutive steps of mechanical stabilisation depending of the vertical displacement ranges.

Increments of vertical displacement (mm)	Ranges of vertical displacement (mm)
$5 \cdot 10^{-3}$	$[0 - 0.1]$
$1 \cdot 10^{-2}$	$[0.1 - 0.4]$
$5 \cdot 10^{-2}$	$[0.4 - 1]$
$1 \cdot 10^{-1}$	$[1 - 3]$
$5 \cdot 10^{-1}$	$[3 - 10]$
1	$[10 - +\infty[$

that since all the units are 3D rigid bodies, each of them has six degrees of freedom (three translations and three rotations), which are expressed at the centre of mass of each unit. With the aim to reproduce the experimental setup, the units of the first masonry course (green and red) were fixed to the platforms (either the fixed (dark grey) or the moving platform (light gray) depending on the unit location). In practice, a Mohr-Coulomb contact with almost infinite strength and stiffness is used in the DEM simulations. In addition, the two platforms are slightly smaller in order to avoid any contact between i) the settling blocks and the fixed platform and ii) the two platforms. Finally, the velocity of the settling platform does not follow the experimental one of Savalle et al. (2023), since the time in the numerical simulation has no real meaning, yet it is taken small enough in order to ensure quasi-static processes (see Section 4.2).

D. Numerical procedure to extract the load-displacement curve

First of all, gravity is applied in one single step and the state of the system under self-weight is computed. Stability is assumed when the maximum velocity of the rigid masonry units is below a given threshold, herein defined to $5 \cdot 10^{-5}\mathrm{m} \cdot \mathrm{s}^{-1}$ thanks to a parametric study (Section 4.2). As the gravity step does not imply any plasticity in the model (i.e. at the dry interfaces), it is noted that the way gravity is applied (one or several steps) should not influence the final state. Then, steps of platform settlement and numerical stabilisation alternate. The platform settles at a constant velocity until a predefined increment of vertical displacement is reached. After, the system is left up to the mechanical stabilisation, here again characterised by a maximum velocity within the masonry wall of $5 \cdot 10^{-5}\mathrm{m} \cdot \mathrm{s}^{-1}$. Once stabilisation is achieved, the vertical position and vertical force (reaction) of the moving platform are recorded. In practice the vertical force is measured as the sum of the vertical forces at each subcontact between the masonry units and the settling platform. Finally, the platform is settling again and another step begins. This procedure continues until failure is achieved, assumed herein when the horizontal displacement of the monitored unit (Figure 3) exceeds $50\mathrm{cm}$. One should note that the load-displacement curves presented in Savalle et al. (2023) are completely non-linear and require much higher precision for small displacement than for larger ones. Therefore, the increments are very small at the beginning of the simulation, while they increase after, see Table 1 for the detailed increments and the associated vertical displacement ranges.

IV. Numerical results

This section now uses the numerical methodology presented above to simulate the experiments of Savalle et al. (2023). It first discusses the material parameters, then some numerical calibrations are conducted. Finally, the numerical and experimental outcomes are compared.

TABLE 2. Material parameters attributed to the numerical DEM model.

Unit weight ($\mathrm{kN \cdot m^{-3}}$)	**Friction** φ **(°)**	**Normal stiffness** k_n ($\mathrm{GPa \cdot m^{-1}}$)	**Tangential stiffness** k_s ($GPa \cdot m^{-1}$)
18.4	33.4	0.342 / 0.570	0.105 / 0.175

A. *Material parameters*

Based on the experimental data of Savalle et al. (2023) and Colombo et al. (2022), Table 2 gathers the material parameters used in the numerical simulations. Though the dry-joint stiffness in general is clearly non-linear with a high impact of the normal stress at the interface (Colombo et al. 2022), DEM numerical studies, including the present work, commonly assume constant dry-joint stiffness values (Bui et al. 2017, Savalle et al. 2020, Funari et al. 2022, Colombo et al. 2022). While the characterisation experiments of Colombo et al. (2022) suggest a value of dry-joint stiffness of $k_n = 1.14\mathrm{GPa \cdot m^{-1}}$ and $k_s = 0.33\mathrm{GPa \cdot m^{-1}}$, their numerical approach employed to replicate their experiments required smaller values, with a proportion of 0.5 or 0.3, which is also in agreement with the findings of Oliveira et al. (2021). In fact, this reduction is attributed to tiny gaps between units that originate from geometrical tolerances. Either a non-perfectly flat surface or two different heights for jointed units generate imperfections in the contact (Oliveira et al. 2021). Importantly, this effect is only observable in a wall, and not in a bilateral contact which is the framework of the characterisation tests conducted in Colombo et al. (2022). Therefore, two values are indicated in Table 2 for the dry-joint stiffness, corresponding to a proportion of 0.5 and 0.3 of the original values $k_n = 1.14\mathrm{GPa \cdot m^{-1}}$ and $k_s = 0.33\mathrm{GPa \cdot m^{-1}}$.

B. *Calibration of the numerical parameters*

The present subsection briefly introduces the numerical calibration conducted for the current simulations for three parameters: a) the settling platform velocity, b) the number of contact points between units and c) the velocity threshold used to define stability in the numerical process (Section 3.4). For each of these three parameters, a parametric analysis on a default case (five units on the settling platform) is conducted and plotted in Figure 4. For brevity, only those cases are shown and discussed, though similar convergences are found for other configurations.

Figure 4a shows that the numerical results converge when the settling velocity is smaller than $5 \cdot 10^{-4}\mathrm{m \cdot s^{-1}}$. By default in 3DEC, only the vertices of each unit constitute potential subcontacts (contact points). In order to improve the accuracy of the transmission of forces, one can add other contact points thanks to a more refined triangulation, based on a characteristic length, which is defined as the the maximum distance between two potential contact points. Here, the reference length is taken as the width of the unit/wall (i.e. $57.3\mathrm{mm}$) and the refinements use a proportion of it (divided by 0.5, 1, 2, 3, 4, 6 and 8). The curves in Figure 4b are sorted from the coarser triangulation to the finer one and one can note that using one-fourth of the reference length ensures very good load transmission, while more contact points do not modify the global response. Therefore, in the following this contact triangulation will be used. Finally, the effect of the velocity threshold is detailed in Figure 4c, where it is observable that if the maximum allowable velocity in the system after mechanical stabilisation is equal (or higher) to $7 \cdot 10^{-4}\mathrm{m \cdot s^{-1}}$, the numerical response is highly unstable. A threshold of $5 \cdot 10^{-5}\mathrm{m \cdot s^{-1}}$ is chosen to produce acceptable results. To conclude, while the effect the number of contact points is relatively high on the numerical computational cost, the effects of

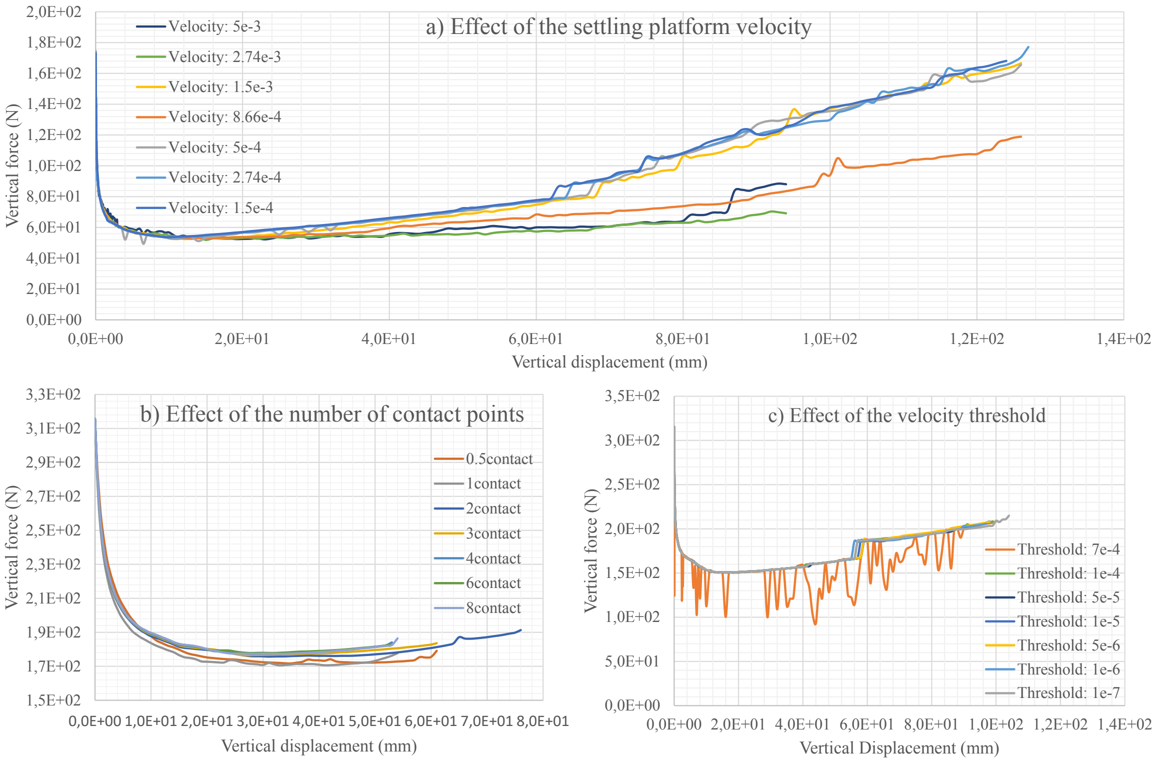

FIGURE 4. Parametric analysis used for the numerical calibration: a) the settling platform velocity (in $\mathrm{m\,cot\,m^{-1}}$), b) the contact point discretisation and c) the velocity threshold (in $\mathrm{m\,cot\,m^{-1}}$) to define stability.

the settling velocity and of the velocity threshold are less critical.

C. *Comparison between numerical and experimental outcomes*

In the last section, experimental and numerical outcomes are compared on two representative configurations of the experimental campaign of Savalle et al. (2023). The first case, denoted as *three units settling* corresponds to the case where three units of the first masonry course are laid on the settling platform while the second case (*five units settling*) has five units of the first masonry course on the settling platform. Five and three experimental tests are available for the two configurations, respectively (Savalle et al. 2023). First, the mechanisms are compared in Figure 5, with two different instants for each configuration and two simulations (one with $k_n = 0.34\mathrm{GPa} \cdot \mathrm{m}^{-1}$ and the other with $k_n = 0.57\mathrm{GPa} \cdot \mathrm{m}^{-1}$, as discussed in Section 4.1). Note that for brevity, only the dry-joint normal stiffness is indicated though the tangential stiffness also follows the values indicated in Table 2. It is first observed a very good agreement in both cases, with only minor differences between the two DEM simulations with the different stiffness. Importantly, the larger stiffness ($k_n = 0.57\mathrm{GPa} \cdot \mathrm{m}^{-1}$) is associated to slightly larger units' displacements while in the smaller stiffness DEM simulation, the deformation of the interfaces (interpenetration) are larger. Yet, overall, the effect of the stiffness on the crack pattern is small.

Figure 6 then compares the load-displacement curves of the two simulations with the experimental

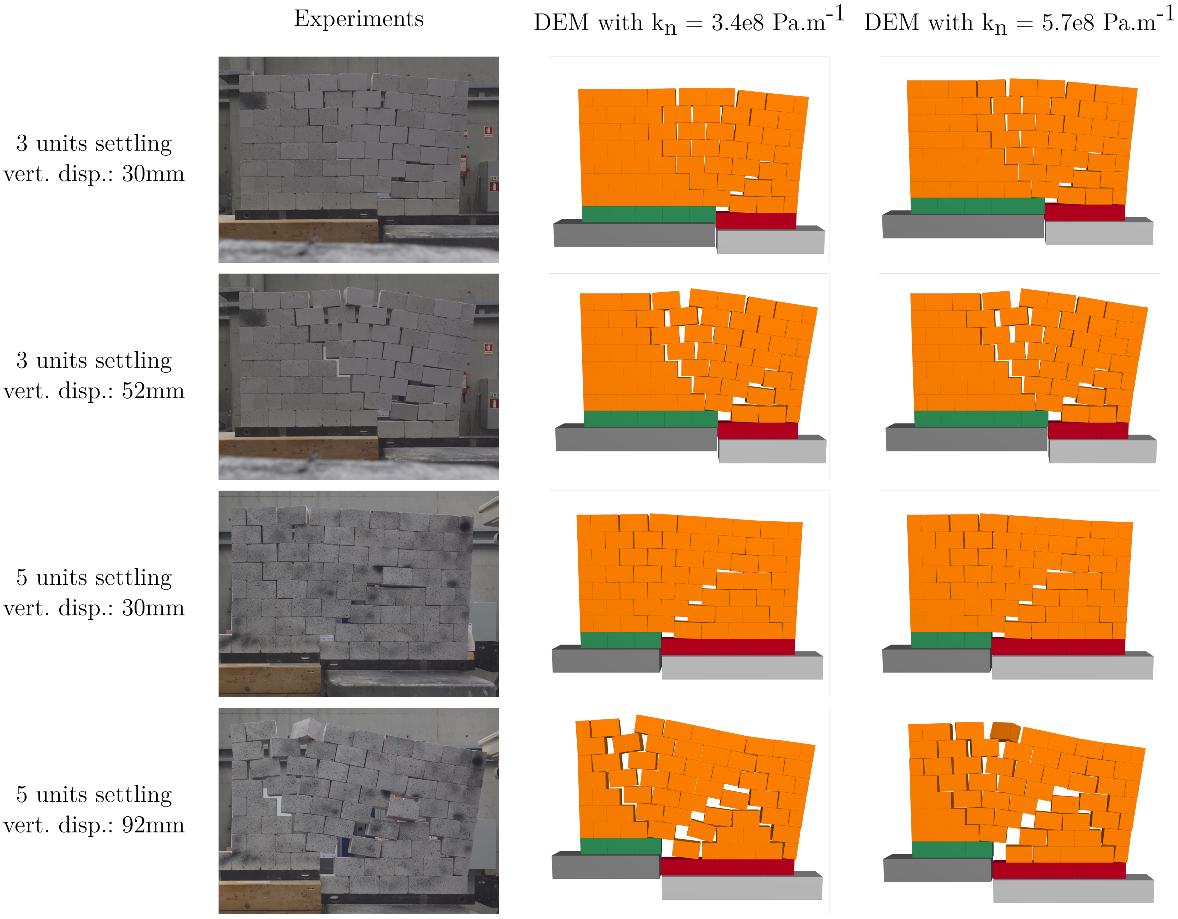

FIGURE 5. Comparison between the failure mechanisms between i) the experiments (Savalle et al. 2023), ii) the DEM simulations with $k_n = 0.34\text{GPa} \cdot \text{m}^{-1}$, and iii) the DEM simulations with $k_n = 0.57\text{GPa} \cdot \text{m}^{-1}$. The comparison is shown for two experiments (three units and five units on the settling platform) at two different instants, herein characterised by the total vertical displacement.

results. First of all, one can note that the first test of the second case (Figure 6b) seems to be an outlier, at least up to 30mm of vertical displacement, and therefore won't be considered in the discussion below. In general, both cases are well replicated through numerical modelling. Again, both values of dry-joint stiffness lead to a very good agreement, though its influence on the numerical results is more visible for the load-displacement curves (Figure 6) than for the crack patterns (Figure 5). In addition, the initial stiffness of the whole structure (i.e. below 5mm) is excellently replicated by the simulations.

In fact, as introduced before (Section 4.1), the dry-joint stiffness properties should also depend on the normal stress acting at the interfaces (Colombo et al. 2022). A simplified approach that considers a constant value for all stresses is only an approximation, which, in the present case, is satisfactory given the very good agreement between experimental and numerical outcomes. Yet, some deviations are still observable between experimental and numerical curves. More importantly, the numerical simulations seem to overestimate the vertical load in the first case (Figure 6a), while they underestimate the vertical load in the second case (Figure 6b). These deviations are attributed to the inherent assumptions of a constant dry-joint stiffness.

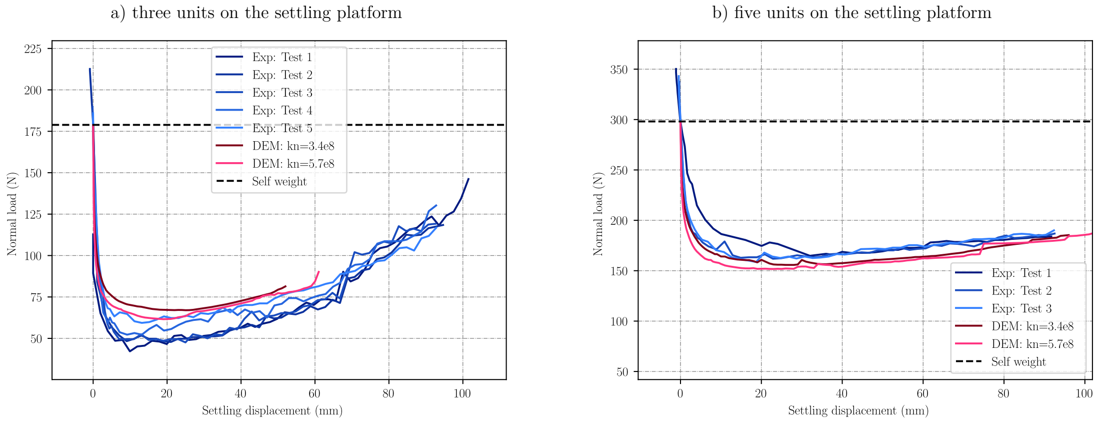
a) three units on the settling platform

b) five units on the settling platform

FIGURE 6. Comparison between the vertical load-displacement curves between i) the experiments (in blue) (Savalle et al. 2023) and ii) the DEM simulations (in red) with $k_n = 0.34\text{GPa}\cdot\text{m}^{-1}$ and $k_n = 0.57\text{GPa}\cdot\text{m}^{-1}$. The comparison is shown for two experiments: (a) three units and (b) five units on the settling platform.

V. Conclusion

The present work details a numerical strategy developed under a 3D discrete element framework to study the settlement of dry-joint masonry buildings. It is tested on a 2D wall but is clearly also applicable to more complex 3D structures. The paper insists on the key aspects of the modelling (on which a potential user should concentrate) and proposes an appropriate procedure. It is then used to replicate experiments on dry-joint masonry shear walls from the literature. Both the failure mechanisms and the vertical load-displacement curves are well predicted. However, the effect of dry-joint stiffness is more important on the load-displacement curves than on the mechanisms. Deviations in the load-displacement curves are attributed to the simplified modelling approach that uses a constant dry-joint stiffness. Indeed, these discrepancies originate from a combination of the following explanations: 1) the dry-joint stiffness should ideally be identified directly on a wall instead of a couplet of masonry units, 2) its value may vary depending on the size and loading condition of the wall and 3) the dry-joint stiffness strongly depends on the normal stress acting at the interface. To conclude, while the collapse mechanism and the load-displacement curve of a settlement experiment are predictable using a classical DEM approach, the perfect match between experimental and numerical curves can only be achieved using a more refined definition of the dry-joint stiffness.

References

Abaqus, . (2014), 'Documentation 651', *Dassault Systemes Simulia Corporation* (6.2).

Alessandri, C., Garutti, M., Mallardo, V. & Milani, G. (2015), 'Crack Patterns Induced by Foundation Settlements: Integrated Analysis on a Renaissance Masonry Palace in Italy', *International Journal of Architectural Heritage* **9**(2), 111–129. Publisher: Taylor & Francis _eprint: https://doi.org/10.1080/15583058.2014.951795.
URL: *https://doi.org/10.1080/15583058.2014.951795*

Alexandris, A., Protopapa, E. & Psycharis, I. (2004), Collapse mechanisms of masonry buildings derived by the distinct element method, *in* 'Proceedings of the 13th world conference on earthquake engineering', p. 14.

Ard, V., Mens, E., Poncet, D., Cousseau, F., Defaix, J., Mathé, V. & Pillot, L. (2015), 'Life and death of Angoumoisin-type dolmens in west-central France', *Bulletin de la Société Préhistorique Française* **113**(4), 737–764.

Bui, T., Limam, A., Sarhosis, V. & Hjiaj, M. (2017), 'Discrete element modelling of the in-plane and out-of-plane behaviour of dry-joint masonry wall constructions', *Engineering Structures* **136**, 277–294.
URL: *https://linkinghub.elsevier.com/retrieve/pii/S0141029617300913*

Ceravolo, R., De Marinis, A., Pecorelli, M. L. & Zanotti Fragonara, L. (2017), 'Monitoring of masonry historical constructions: 10 years of static monitoring of the world's largest oval dome', *Structural Control and Health Monitoring* **24**(10), e1988. Publisher: Wiley Online Library.

Chen, X., Wang, X., Wang, H., Agrawal, A. K., Chan, A. H. & Cheng, Y. (2021), 'Simulating the failure of masonry walls subjected to support settlement with the combined finite-discrete element method', *Journal of Building Engineering* p. 102558. Publisher: Elsevier.

Colombo, C., Savalle, N., Mehrotra, A., Funari, M. F. & Lourenço, P. B. (2022), 'Experimental, numerical and analytical investigations of masonry corners: Influence of the horizontal pseudo-static load orientation', *Construction and Building Materials* **344**, 127969.
URL: *https://www.sciencedirect.com/science/article/pii/S0950061822016397*

Cousseau, F. (2016), Archéologie du bâti mégalithique dans l'ouest de la France, PhD Thesis, Rennes 1.

Cundall, P. A. (1971), A computer model for simulating progressive large-scale movements in blocky rock systems, *in* 'Proceedings of the Symposium of the International Society for Rock Mechanics, Nancy, France', Vol. 2.

Dalgic, K. D., Gulen, D. B., Acikgoz, S., Burd, H., Hendriks, M. A., Giardina, G. & Ilki, A. (2021), Large scale experimental settlement tests to evaluate structural models for tunnelling-induced damage analysis, *in* 'International Conference of the International Association for Computer Methods and Advances in Geomechanics', Springer, pp. 164–171.

D'Altri, A. M., De Miranda, S., Castellazzi, G., Sarhosis, V., Hudson, J. & Theodossopoulos, D. (2019), 'Historic barrel vaults undergoing differential settlements', *International Journal of Architectural Heritage* . Publisher: Taylor & Francis.

Deck, O. & Singh, A. (2012), 'Analytical model for the prediction of building deflections induced by ground movements', *International Journal for Numerical and Analytical Methods in Geomechanics* **36**(1), 62–84. Publisher: Wiley Online Library.

European Comission (2010), Europe, the world's No 1 tourist destination – a new political framework for tourism in Europe, Communication from the Commission to the European Parliament, the Council, the European Economic and Social Committee and the Committee of the Regions COM/2010/0352.

Funari, M. F., Hajjat, A. E., Masciotta, M. G., Oliveira, D. V. & Lourenço, P. B. (2021), 'A Parametric Scan-to-FEM Framework for the Digital Twin Generation of Historic Masonry Structures', *Sustainability* **13**(19), 11088. Publisher: Multidisciplinary Digital Publishing Institute.

Funari, M. F., Silva, L. C., Savalle, N. & Lourenço, P. B. (2022), 'A concurrent micro/macro FE-model optimized with a limit analysis tool for the assessment of dry-joint masonry structures', *International Journal for Multiscale Computational Engineering* **20**(5), 65–85. Publisher: Begel House Inc.
URL: *https://www.dl.begellhouse.com/journals/61fd1b191cf7e96f,forthcoming,40212.html*

Gagliardo, R., Portioli, F. P. A., Cascini, L., Landolfo, R. & Lourenço, P. B. (2021), 'A rigid block model with no-tension elastic contacts for displacement-based assessment of historic masonry structures subjected to settlements', *Engineering Structures* **229**, 111609.

Giardina, G., Marini, A., Hendriks, M. A., Rots, J. G., Rizzardini, F. & Giuriani, E. (2012), 'Experimental analysis of a masonry façade subject to tunnelling-induced settlement', *Engineering Structures* **45**, 421–434. Publisher: Elsevier.

Giardina, G., Marini, A., Riva, P. & Giuriani, E. (2020), 'Analysis of a scaled stone masonry facade subjected to differential settlements', *International Journal of Architectural Heritage* **14**(10), 1502–1516. Publisher: Taylor & Francis _eprint: https://doi.org/10.1080/15583058.2019.1617911.
URL: *https://doi.org/10.1080/15583058.2019.1617911*

Giardina, G., Van de Graaf, A. V., Hendriks, M. A., Rots, J. G. & Marini, A. (2013), 'Numerical analysis of a masonry façade subject to tunnelling-induced settlements', *Engineering structures* **54**, 234–247. Publisher: Elsevier.

Hemeda, S. (2021), 'Numerical analysis of geotechnical problems of historic masonry structures', *Geotechnical and Geological Engineering* **39**(3), 2461–2469. Publisher: Springer.

Itasca (2019), *3 Dimensional Distinct Element Code (3DEC) : Theory and background, 7th Edition*, Itasca Consulting Group.

Jaiswal, K. & Wald, D. J. (2008), *Creating a global building inventory for earthquake loss assessment and risk management*, U.S. Geological Survey, Open-File Report 2008-1160.

Laefer, D. F., Hong, L. T., Erkal, A., Long, J. H. & Cording, E. J. (2011), 'Manufacturing, assembly, and testing of scaled, historic masonry for one-gravity, pseudo-static, soil-structure experiments', *Construction and Building Materials* **25**(12), 4362–4373.
URL: *http://www.sciencedirect.com/science/article/pii/S0950061811001310*

Lemos, J. V. (2007), 'Discrete Element Modeling of Masonry Structures', *International Journal of Architectural Heritage* **1**(2), 190–213.
URL: *http://www.tandfonline.com/doi/abs/10.1080/15583050601176868*

Lemos, J. V. (2019), 'Discrete Element Modeling of the Seismic Behavior of Masonry Construction', *Buildings* **9**(2), 43.

Masciotta, M.-G., Ramos, L. F. & Lourenço, P. B. (2017), 'The importance of structural monitoring as a diagnosis and control tool in the restoration process of heritage structures: A case study in Portugal', *Journal of Cultural Heritage* **27**, 36–47. Publisher: Elsevier.

Milani, G., Esquivel, Y. W., Lourenço, P. B., Riveiro, B. & Oliveira, D. V. (2013), 'Characterization of the response of quasi-periodic masonry: Geometrical investigation, homogenization and application to the Guimarães castle, Portugal', *Engineering structures* **56**, 621–641. Publisher: Elsevier.

Mithen, S. (2011), *After the ice: a global human history, 20,000-5000 BC*, Weidenfeld & Nicolson.

Oliveira, R. L., Rodrigues, J. P. C., Pereira, J. M., Lourenço, P. B. & Marschall, H. U. (2021), 'Normal and tangential behaviour of dry joints in refractory masonry', *Engineering Structures* **243**, 112600. Publisher: Elsevier.

Portioli, F. & Cascini, L. (2016), 'Assessment of masonry structures subjected to foundation settlements using rigid block limit analysis', *Engineering Structures* **113**, 347–361. Publisher: Elsevier.

Portioli, F. & Cascini, L. (2017), 'Large displacement analysis of dry-jointed masonry structures subjected to settlements using rigid block modelling', *Engineering Structures* **148**, 485–496. Publisher: Elsevier.

Ramírez, P. B., de Balbín Behrmann, R., Laporte, L., Gouézin, P., Cousseau, F., Bermejo, R. B., Gismero, A. H., Cela, M. I. & Quesnel, L. (2015), 'Natural and artificial colours: the megalithic monuments of Brittany', *Antiquity* **89**(343), 55–71.

Ritter, S., Giardina, G., DeJong, M. J. & Mair, R. J. (2018), 'Centrifuge modelling of building response to tunnel excavation', *International Journal of Physical Modelling in Geotechnics* **18**(3), 146–161. Publisher: Thomas Telford Ltd.

Savalle, N., Funari, M. F., Fernandes, L., Colombo, C., Szabó, S., Hussaini, S., Karimzadeh, S. & Lourenco, P. B. (2023), Large static testing equipment: design and testing of a settlement facility, *in* 'Testing and Experimentation in Civil Engineering - From Current to Smart Technologies', Lisbon, Portugal.

Savalle, N., Lourenço, P. B. & Milani, G. (2022), 'Joint Stiffness Influence on the First-Order Seismic Capacity of Dry-Joint Masonry Structures: Numerical DEM Investigations', *Applied Sciences* **12**(4), 2108. Publisher: Multidisciplinary Digital Publishing Institute.

Savalle, N., Vincens, r. & Hans, S. (2020), 'Experimental and numerical studies on scaled-down dry-joint retaining walls: Pseudo-static approach to quantify the resistance of a dry-joint brick retaining wall', *Bulletin of Earthquake Engineering* **18**, 581–606.
URL: *https://doi.org/10.1007/s10518-019-00670-9*

Stepinac, M., Lourenço, P. B., Atalić, J., Kišiček, T., Uroš, M., Baniček, M. & Šavor Novak, M. (2021), 'Damage classification of residential buildings in historical downtown after the ML5.5 earthquake in Zagreb, Croatia in 2020', *International Journal of Disaster Risk Reduction* **56**, 102140.
URL: *https://www.sciencedirect.com/science/article/pii/S2212420921001060*

Vlachakis, G., Vlachaki, E. & Lourenço, P. B. (2020), 'Learning from failure: Damage and Failure of Masonry Structures, after the 2017 Lesvos Earthquake (Greece)', *Engineering Failure Analysis* p. 104803. Publisher: Elsevier.

Xiao, S., Li, N. & Guo, X. (2021), 'Analysis of flood impacts on masonry structures and mitigation measures', *Journal of Flood Risk Management* **14**(4), e12743. Publisher: Wiley Online Library.